**ELECTRONIC SUPPLEMENTARY INFORMATION**

# Controlled Synthesis of Solid-Shelled Non-Spherical and Faceted Microbubbles

*Seon Ju Yeo,‡[a] Min Jun Oh,‡[b] Youngsoo Kim,[a] Byung Mook Weon,[c] S. Joon Kwon*[d,e] and Pil J. Yoo*[d,e,f]*

[a.] Deparment of Nature-Inspired System and Application
Korea Institute of Machinery & Materials (KIMM), Daejeon 34103, Republic of Korea

[b.] Department of Chemical and Biomolecular Engineering,
University of Pennsylvania, Philadelphia, Pennsylvania 19104, USA

[c.] School of Advanced Materials Science and Engineering,
Sungkyunkwan University (SKKU), Suwon 16419, Republic of Korea

[d.] School of Chemical Engineering,
Sungkyunkwan University (SKKU), Suwon 16419, Republic of Korea

[e.] SKKU Institute of Energy Science and Technology (SIEST),
Sungkyunkwan University (SKKU), Suwon 16419, Republic of Korea

[f.] SKKU Advanced Institute of Nanotechnology (SAINT),
Sungkyunkwan University (SKKU), Suwon 16419, Republic of Korea

‡ Euqal contribution.

* Email: sjoonkwon@skku.edu; pjyoo@skku.edu

## Experimental Section

### Synthesis of alkylated graphene oxide

Negatively charged graphene oxide (GO) nanosheets were synthesised using a modified Hummers' method, as previously reported.[1] For the alkylation of GOs, 2.0 g of 1-ethyl-3-(3-dimethylaminopropyl)carbodiimide and hydrochloride (EDC) were first added to 400 mL of GO (0.5 mg $mL^{-1}$). Octadecylamine (ODA, 2.0 g) was added to the GO solution and then reacted by vigorous stirring at room temperature for 1 day. After completion of the reaction, the solution was rinsed several times with deionized (DI) water or ethanol and then dried at 70 °C. Lightly alkylated GOs (L-GOs) were redispersed in toluene at a targeted concentration (15 mg $mL^{-1}$).

### Generation of non-spherical bubbles with capillary microfluidic devices

Gas-in-oil-in-water (G/O/W) compound bubbles were prepared using a glass capillary microfluidic device, as previously described.[2] Briefly, two round capillary tubes with inner and outer diameters of 0.58 mm and 1.0 mm (1B100-6, World Precision Instrument Inc.), respectively, which were tapered by a micropipette puller (P-1000, Sutter Instrument Inc.) and microforge (MF-830, Narishige), were coaxially aligned in a square capillary tube (inner diameter 1.05 mm, Harvard borosilicate square tubing). The tapered capillaries had ~5 and 180 μm orifices for injection and collection tubes, respectively. A round capillary tube used for the injection was treated with octadecyltrichlorosilane (OTS) for 30 min at 150 °C to render the surfaces hydrophobic. The inner gas ($N_2$) was introduced into a microfluidic device via a pressure regulator (NEW-FLOW DPG3000, New-Flow Technologies, Inc.), and the middle and outer phases were injected into the device with syringe pumps (KDS 100, KD Scientific). The flow rates for the inner phase (G), middle phase (O), and outer phase (W) were precisely adjusted to control the size and shell thickness of the bubbles. The resulting G/O/W compound bubbles were incubated in a poly(vinyl alcohol) (PVA) aqueous solution at room temperature to evaporate the organic solvent.

### Characterization

The production of G/O/W compound bubbles was monitored with an inverted microscope (Nikon Eclipse Ti-U) equipped with a high-speed camera (Phantom M100). The generated bubbles were observed and imaged using an optical microscope (Olympus BX60) with a charge-coupled device camera (Nikon DS-Fi3). Scanning electron microscopy (SEM) images were acquired using a JSM-7401F (JEOL). X-ray nanotomography (XNT) images of the microbubbles were taken using the 7C X-ray Nano Imaging (XNI) beamline (photo energy ~ 6.7 keV) at the Pohang Light Source II (PLS-II). The alkylated GO nanosheets were examined by atomic force microscope (AFM, Dimension 3100, Veeco, Plainview, USA).

### Code availability

The MATLAB scripts used to calculate the shell deformation of L-GO-shelled microbubbles are available from the corresponding author upon reasonable request.

## S1. Calculation of the degree of alkylation of GOs

The degree of alkylation of the alkylated GOs can be estimated based on C/O ratio because C/O ratio is not affected directly by other impurities. As shown in Table S1, the C/O ratio is 5.26 for L-GO and 23.1 for H-GO. Assuming that the chemical structure of GO nanosheet is $C_{12}O_2(OH)_2(COOH)_1$, the degree of alkylation of L-GO and H-GO can be calculated to be 26.57% and 101.76%, respectively. The degree of alkylation greater than 100% indicates that the carboxyl groups in the GO nanosheets are completely alkylated.

## S2. Determination of the imposed direction of the Laplace pressure at the triple interface

In microbubbles with a shell composed of H-GO platelets, the shell does not support the Laplace pressure acting inward. This is attributed to the fact that the evaporation of toluene from the spherical cap of the microbubble with H-GO shells is distinctively slower than that from the microbubble with L-GO (Fig. 3). For H-GO, the higher number density of octadecylamine chains allows H-GO to more effectively accommodate toluene, showing a better dispersion and slower rate of solvent evaporation than L-GO (Fig. S1). This difference in the accommodating capacity of toluene between H-GO and L-GO is clear in the experimental observation of the size reduction of H-GO and L-GO dispersed droplets (Fig. 3 and Movie S3). For H-GO, it can be assumed that $\gamma_{SA} \sim \gamma_{OA} =$ 28.5 mN m$^{-1}$ and $\gamma_{SW} \sim \gamma_{OW} =$ 55.8 mN m$^{-1}$, where $\gamma_{OA}$ and $\gamma_{OW}$ denote the interface energies between toluene/air and toluene/water, respectively. In contrast, for L-GO, $\gamma_{SA} \sim \gamma_{GA} =$ 38.4 mN m$^{-1}$ (detailed in Fig. S4, Table S2, and Section S3) and $\gamma_{SW} \sim \gamma_{GW} =$ 6.16 mN m$^{-1}$, where $\gamma_{GA}$ and $\gamma_{GW}$ are the interface energies between GO/air and GO/water, respectively.[3,4] From this comparison, one can find that $2(\gamma_{SA} - \gamma_{SW})/R < 0$ for microbubbles with a shell of H-GO, whereas $2(\gamma_{SA} - \gamma_{SW})/R > 0$ for microbubbles with a shell of L-GO. Therefore, microbubbles with a shell of L-GO would undergo shape deformation triggered by the Laplace pressure acting inward from the bubble.

## S3. Calculation of surface tension of alkylated GOs

We used Neumann model to calculate the surface energy of the alkylated GO films from contact angle data. Based on Neumann's equation of state theory, the contact angle ($\theta$) between the solid surface and liquid is given as follows:[3,4]

$$\cos\theta = -1 + 2\sqrt{\frac{\gamma_s}{\gamma_l}}e^{-\beta(\gamma_s-\gamma_l)^2}$$

where $\gamma_s$ and $\gamma_l$ are solid and liquid free surface energy, respectively, and $\beta$ is the constant coefficient related to the solid surface. Then, the following equation can be derived:

$$\ln\left[\gamma_l\left(\frac{1+\cos\theta}{2}\right)^2\right] = -2\beta(\gamma_s-\gamma_l)^2 + \ln(\gamma_s).$$

Average contact angle data for the five different polar solvents are shown in Table S2. The liquid surface energy is already known, and plotting the left side of the equation against $\gamma_l$ can allow us to determine the solid surface energy by means of a parabolic curve of data points: the surface energies of L-GOs and H-GOs at room temperature are 38.43 and 34.53 mJ $m^{-2}$, respectively (Fig. S4). In our case, the surface roughness has no significant effect on the contact angle and thus, the calculated surface energy.

## Supplementary figures:

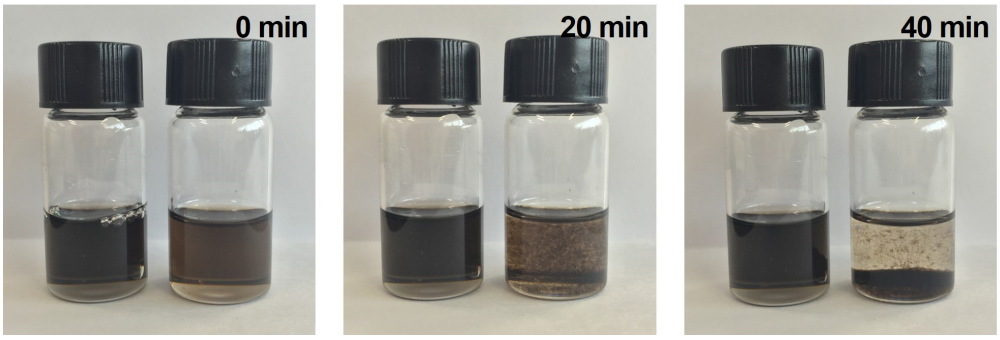


**Figure S1.** Photographs showing the different dispersibility of H-GOs (left) and L-GOs (right) dispersed in toluene after sonication. The concentration of GO solution is adjusted to 0.4 mg $mL^{-1}$.

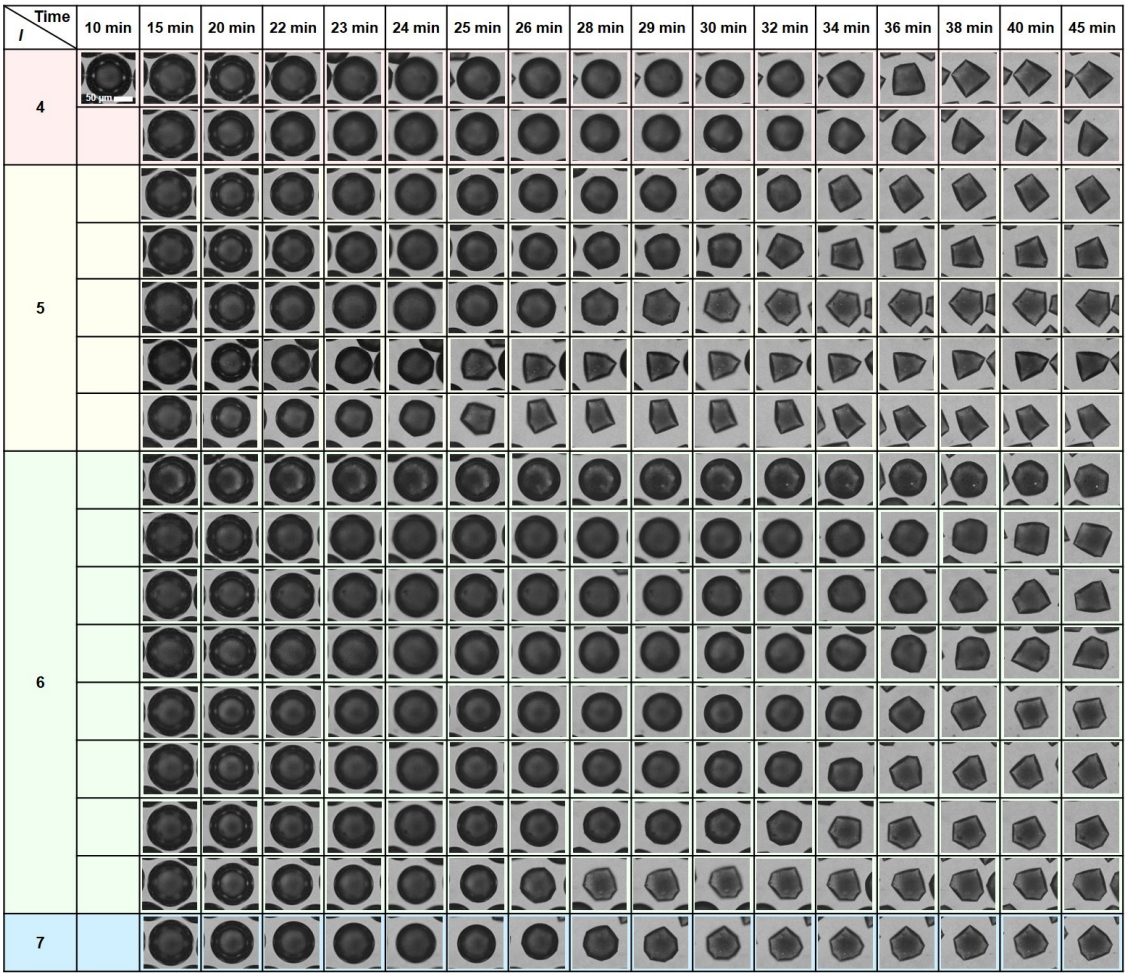


**Figure S2.** Time-lapse OM images of the detailed sphere-to-polytope deformation processes of 16 non-spherical bubbles containing L-GOs over time winding up with the convex polyhedral bubbles with different mode numbers ($l$ = 4–7).

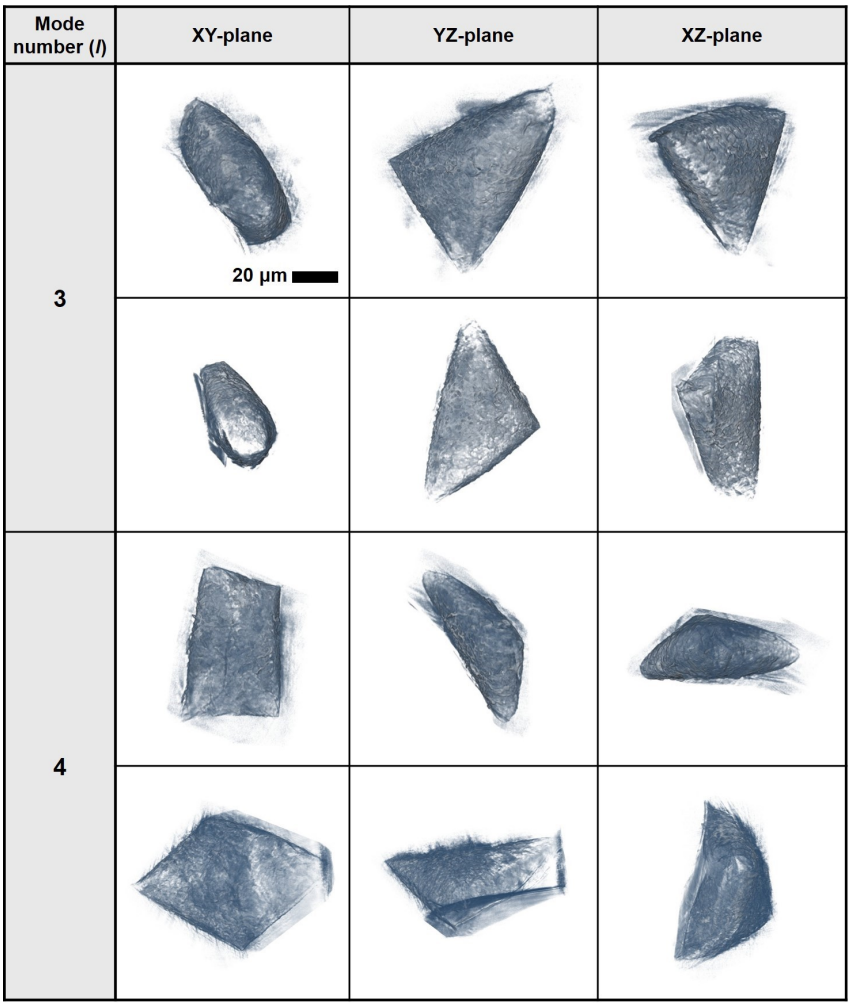


**Figure S3.** Snapshots of the XNT images of the convex polytope-shaped microbubbles with the mode numbers ($l$) of 3 and 4 taken at different points of views. The detailed information of the 3D shape of the bubbles can be found in Movie S2.

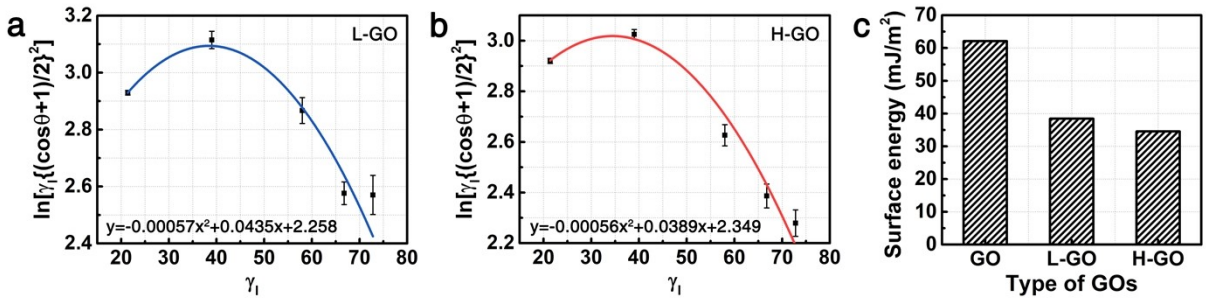


**Figure S4.** (a,b) Plots of $\ln\left[\gamma_l\left\{(\cos\theta+1)/2\right\}^2\right]$ as a function of $\gamma_l$ for (a) L-GO and (b) H-GO thin film. We used Neumann model to calculate the surface energy from contact angle ($\theta$) data. $\gamma_s$ and $\gamma_l$ represent solid and liquid free surface energy, respectively. (c) Surface energies with respect to the degree of alkylation of GOs.

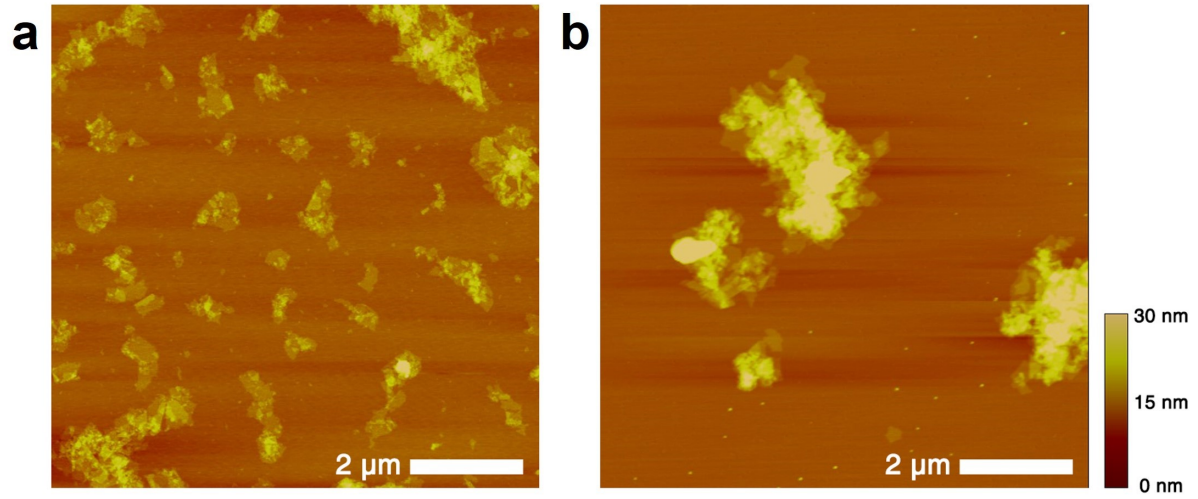


**Figure S5.** Height-mode atomic force microscopy (AFM) observation of (a) H-GO and (b) L-GO nanosheets. The toluene solutions containing either H-GOs or L-GOs are spin-coated onto a silicon wafer at 1500 rpm for 30 s. The *z*-scale is 30 nm. The H-GO solution leaves thin layers of exfoliated GO nanosheets with a thickness of ~2 nm, whereas the L-GO solution forms randomly agglomerated GO nanosheets with a broad thickness distribution ranging from 2 to 40 nm. Notably, well-dispersed alkylated GO nanosheets (H-GOs) easily slip over each other and rearrange themselves into a uniformly stacked shell; this minimises the stress generated by the solvent evaporation process. However, for the aggregated GO sheets (L-GOs), interlayer slipping is relatively suppressed; thus, the compressive stress generated during solvent evaporation gradually accumulates within the middle layer.

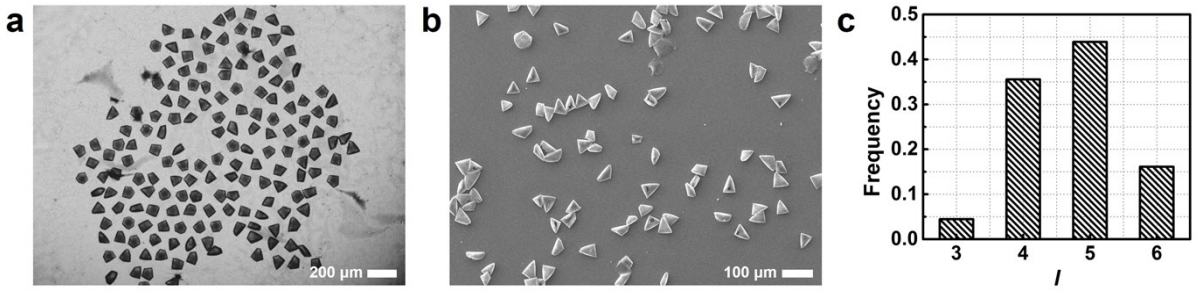


**Figure S6.** OM images of (a) convex polytope-shaped microbubbles after shape deformation (completed after 45 min). (b) SEM images of convex polytope-shaped microbubbles. (c) A distribution of frequency of the experimentally observed spherical mode numbers of the bubbles.

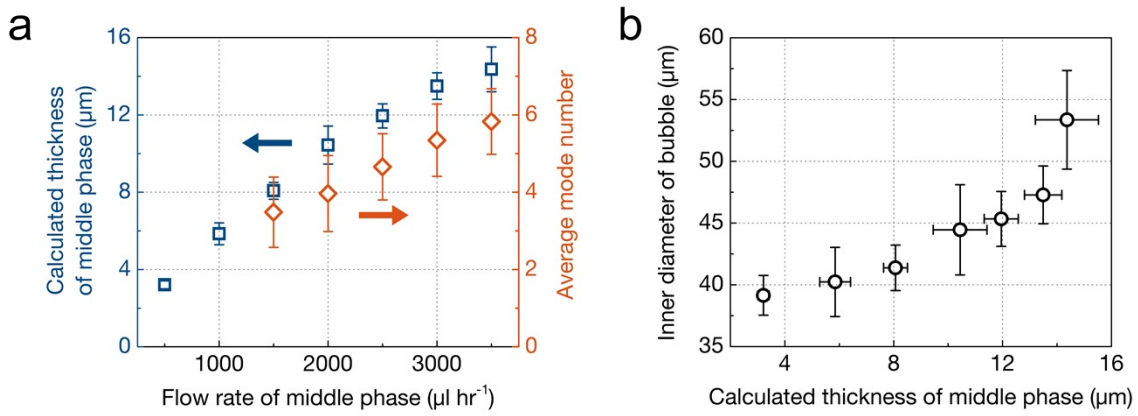


**Figure S7.** (a) Effect of the flow rate of the middle phase on the shell thickness of the compound bubbles and average mode number. The flow rate of the outer phase was kept constant at 80 ml $hr^{-1}$ and the inner gas pressure was maintained at 1.08 bar. (b) The inner diameter of the bubble as a function of the calculated thickness of the middle phase.

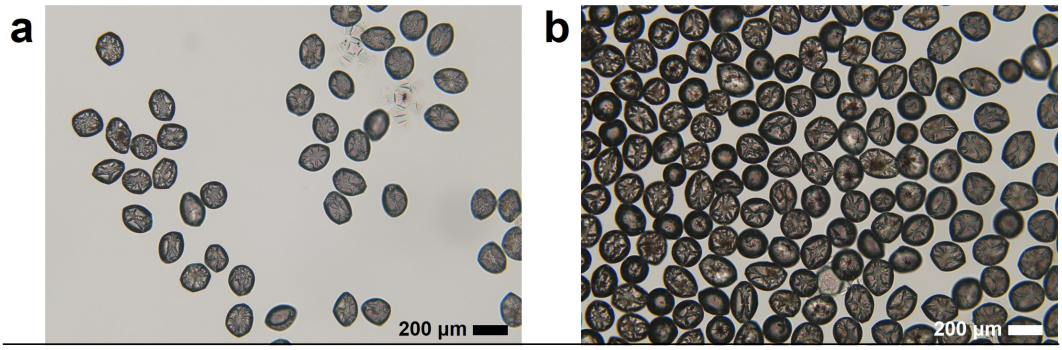


**Figure S8.** OM images of the generation of crumpled bubbles under the middle flow rate of (a) 500 μL $h^{-1}$ and (b) 1000 μL $h^{-1}$.

**Table S1.** Atomic compositions of carbon (C), oxygen (O), and nitrogen (N), as well as the C/O ratio, obtained from XPS spectra of L-GO and H-GO.

| | **C (conc%)** | **O (conc%)** | **N (conc%)** | **C/O ratio** |
|---|---|---|---|---|
| **L-GO** | 81.90 | 15.58 | 2.52 | 5.26 |
| **H-GO** | 94.57 | 4.10 | 1.33 | 23.05 |

**Table S2.** Surface energy of various polar solvents and average contact angles ($\theta_c$) of the solvents on the surface of L-GO and H-GO films. Numbers in parentheses denote the standard deviation.

| | **Water** | **Glycerol solution** | **Formamide** | **Benzyl alcohol** | **Ethanol** |
|---|---|---|---|---|---|
| **Surface energy (mJ m$^{-2}$)** | 72.8 | 66.8 | 58.0 | 39.0 | 21.4 |
| **$\theta_c$ of droplets on L-GO film** | 98.75° (1.687°) | 96.46° (1.022°) | 84.18° (1.417°) | 58.65° (1.547°) | 29.51° (0.875°) |
| **$\theta_c$ of droplets on H-GO film** | 105.5° (1.140°) | 101.1° (1.121°) | 91.33° (1.172°) | 63.03° (0.889°) | 30.46° (1.079°) |

## Supplementary Movies:

**Movie S1**. A movie of time-lapse OM images of the sphere-to-polytope shape deformation of G/O/W compound bubbles containing L-GOs.

**Movie S2**. An XNT imaging movie of convex polytope-shaped microbubbles composed of L-GOs with the mode numbers (*l*) of 3.

**Movie S3**. The wetting and interfacial behaviour of toluene droplets contianig GOs (top) and alkylated GOs (H-GOs (bottom left) and L-GOs (bottom right)) at planar air-water interface in the course of the solvent evaporation.

## References:


1. Y. Zhu, S. Murali, W. Cai, X. Li, J. W. Suk, J. R. Potts and R. S. Ruoff, *Adv. Mater.*, 2010, **22**, 3906−3924.
2. S. J. Yeo, M. J. Oh, H. M. Jun, M. Lee, J. G. Bae, Y. Kim, K. J. Park, S. Lee, D. Lee, B. M. Weon, W. B. Lee, S. J. Kwon and P. J. Yoo, *Adv. Mater*., 2018, **30**, 1802997.
3. S. Wang, Y. Zhang, N. Abidi and L. Cabrales, *Langmuir*, 2009, **25**, 11078−11081.
4. A. Kozbial, Z. Li, C. Conaway, R. McGinley, S. Dhingra, V. Vahdat, F. Zhou, B. D'Urso, H. Liu and L. Li, *Langmuir*, 2014, **30**, 8598−8606.